JGR Space Physics

RESEARCH ARTICLE
10.1029/2020JA028709

Key Points:

- Distinct effects of various seismic source parameters such as vertical surface displacement, magnitude and focal depth on coseismic ionospheric perturbation (CIP) amplitudes
- Amplitudes of coseismic ionospheric perturbations strongly depend on maximum vertical surface displacement
- Deep earthquakes are less efficient in generating detectable CIPs

Supporting Information:

- Table S1

Correspondence to:
A. S. Sunil,
sunnil.as@gmail.com

Citation:
Sunil, A. S., Bagiya, M. S., Bletery, Q., & Ramesh, D. S. (2021). Association of ionospheric signatures to various tectonic parameters during moderate to large magnitude earthquakes: Case study. *Journal of Geophysical Research: Space Physics*, *126*, e2020JA028709. https://doi.org/10.1029/2020JA028709

Received 13 SEP 2020
Accepted 9 FEB 2021

Association of Ionospheric Signatures to Various Tectonic Parameters During Moderate to Large Magnitude Earthquakes: Case Study

A. S. Sunil[1], Mala S. Bagiya[1], Quentin Bletery[2], and D. S. Ramesh[1]

[1]Indian Institute of Geomagnetism (DST), Navi Mumbai, India, [2]Université Côte d'Azur, IRD,CNRS, Observatoire de la Côte d'Azur, Géoazur, Valbonne, France

Abstract The sudden ground movement associated with Mw > 6.5 earthquakes is considered a potential source of ionospheric electron density perturbations over the fault region. Coseismic ground displacement is a function of various seismic source parameters such as moment magnitude, focal depth, and focal mechanism etc. We study here the distinct effects of vertical ground displacement, moment magnitude and focal depth on coseismic ionospheric perturbation (CIP) amplitudes during moderate-to-large earthquakes. We analyze GPS-total electron content variations during 59 dip-slip earthquakes that occurred in the last 20 years. Our study reveals that though CIP amplitudes are primarily controlled by moment magnitude, they are also sensitive to the earthquake focal depth. To understand the influence of focal depth on the displacement field and therefore on CIP amplitudes, we present a simple synthetic test, for a depth range of 0–200 km, highlighting that the maximum vertical ground displacement decreases logarithmically with increasing focal depth while the volume (i.e., integrated vertical ground displacement) of uplifted/subsided material varies very marginally. We conclude that CIP is sensitive to the wavelength of co-seismic vertical displacement field and that seismic energy propagation to the overlying atmosphere during deep earthquakes is not adequate to generate detectable CIP.

Plain Language Summary A small part of energy released during earthquakes transfer to the atmosphere in terms of mechanical waves. For large magnitude earthquakes (generally Mw > 6.5), the atmospheric amplification of such seismically induced waves can generate disturbances in ionospheric electron density termed as Coseismic Ionospheric Perturbations (CIP). The moment magnitude of earthquakes mainly controls the amplitude of ionospheric perturbations. In this study, the effect of focal depth on CIP amplitudes are investigated. The analysis of 59 dip-slip earthquakes shows that deep earthquakes generate smaller CIP amplitudes. The sudden ground movement during earthquakes is responsible for the transfer of seismic energy to the atmosphere. Our study shows that CIP amplitudes are not only sensitive to earthquake magnitude but also to their focal depth. Though the integrated displacement field is insensitive to the earthquake depth, its distribution is very different, concentrated in a narrow area for shallow earthquakes, spread over a wide region for deep earthquakes. CIP amplitudes appear to scale with the maximum values of vertical surface displacement rather than their average. Thus, the energy transfer is more efficient during shallow earthquakes.

1. Introduction

The manifestation of Coseismic Ionospheric Perturbations (CIP) depends on the (1) manifestations of seismic forcing at the Earth surface, (2) acoustic impedance contrast between the solid Earth and atmosphere, and (3) prevailing nontectonic forcing mechanisms at ionospheric altitudes. The coseismic ground displacements surrounding the epicenter can perturb the nearby atmosphere by transferring part of the induced seismic energy. This seismic energy input acts as a main source of near-field CIP and thus the CIP characteristics predominantly depend on seismic source parameters such as the earthquake magnitude, focal depth, focal mechanism, surface deformation, rupture propagation direction etc (Astafyeva & Heki, 2009; Bagiya et al., 2017, 2018, 2019; Cahyadi & Heki, 2015; Heki et al., 2006; Perevalova et al., 2014; Rolland et al., 2013; Sunil et al., 2017). The acoustic impedance contrast between the solid Earth and atmosphere is of the order of 10^{-4} which allows the transfer of a small part of seismic energy (about 10^{-4}–10^{-5}) to the atmosphere in the infrasonic acoustic frequency domain (Lognonné &

Garcia, 2006; Lognonné et al., 1998; Watada & Kanamori, 2010). The energy transfer is maximum at the acoustic resonance frequencies of ∼3.7 and ∼4.4 mHz (Lognonné et al., 1998; Rolland et al., 2011). When the seismically induced acoustic waves propagate to the ionosphere, their amplitude and phase vary according to the nontectonic forcing mechanisms due to geomagnetic field and background ionization density that prevail at ionospheric altitudes. The recording of CIP is also sensitive to the observation geometry of satellite measurement system. The geomagnetic field mainly favors the equatorward propagation of CIP and thus introduces directional asymmetry in their evolution (Bagiya et al., 2017, 2019; Heki & Ping, 2005; Sunil et al., 2017). In addition to that, higher background ionization density leads to higher CIP amplitudes and vice versa (Bagiya et al., 2019). Moreover, when the CIP are recorded using various Global Navigation Satellite Systems (GNSS), the satellite geometry can introduce observation biases (Bagiya et al., 2017, 2019; Georges & Hooke, 1970).

First report on seismic induced ionospheric perturbations was documented after the Mw 9.2, March 28, 1964 Alaska earthquake (Davies & Baker, 1965). The study attributed the cause of perturbations to the pressure waves generated by coseismic crustal movement. After the commencement of GPS, the first study using the GPS-total electron content (TEC) measurement technique was credited to the detection of CIP associated with the Mw 6.7, January 17, 1994 Northridge earthquake. The detected ionospheric electron density perturbations were attributed to the strong ground displacements during this event (Calais & Minster, 1995). A number of subsequent studies could establish the link between coseismic ground displacements and CIP characteristics (Heki et al., 2006; Rolland et al., 2013; Sunil et al., 2017). It was also shown that the CIP amplitudes associated with dip-slip earthquakes were higher than that of strike-slip earthquakes due to the associated higher vertical displacements (uplift/subsidence) (Astafyeva et al., 2014; Perevalova et al., 2014). Thereby, co-seismic crustal deformations play a very important role in generating the subsequent ionospheric perturbations. Coseismic crustal deformation is a function of earthquake source parameters such as magnitude, depth, focal mechanism etc (Bonilla, 1988; Wells & Coppersmith, 1994). Thus, the CIP characteristics may also contain the effects of these earthquake source parameters.

Few studies have been carried out to examine these effects. Astafyeva and Heki (2009) reported the dependence of near-field CIP on focal mechanisms and showed that the polarity of ground deformation (uplift/subsidence) dictates the initial phase of CIP. Astafyeva et al. (2013) studied the CIP amplitudes associated with shallow earthquakes (focal depth between 12 and 55 km) and reported that larger magnitude earthquakes generate larger CIP amplitudes. Their study was focused on reverse fault mechanism events only. Cahyadi and Heki (2015) analyzed the CIP amplitudes during 21 events, including both dip-slip and strike-slip events and derived an empirical scaling law between the CIP amplitudes and moment magnitudes. They also found that strike-slip earthquakes negatively deviate from the derived law. CIP amplitudes depend on the moment magnitude, thus, the detection of CIP may become difficult below certain magnitudes. Perevalova et al. (2014) analyzed the ionospheric responses to earthquakes with moment magnitudes (Mw) between 4.1 and 8.8. They reported a detection threshold magnitude at ∼Mw 6.5, meaning that Mw > 6.5 earthquakes are likely to produce detectable ionospheric perturbations.

As aforesaid, the earthquake magnitudes and corresponding CIP amplitudes correlate very well. However, during same magnitude events, the CIP amplitudes can differ due to other source properties such as the depth, focal mechanism etc. So far, the dependence of CIP characteristics on earthquake source parameters other than magnitude and focal mechanism has not been investigated in detail. In this study, we focus on (1) the distinct effects of maximum vertical ground displacements, moment magnitude and focal depth on CIP amplitudes and (2) the threshold of seismic energy amplification in the atmosphere to generate detectable electron density perturbations. Moving a step further, we model the variation of the maximum and integrated coseismic ground displacement field for different focal depths. Earlier studies considered strong (Mw 6–6.9), major (Mw 7–7.9) and great (Mw > 8) earthquakes together to establish the link between seismic source parameters and CIP characteristics (Astafyeva et al., 2013; Cahyadi & Heki, 2015). The great earthquakes produce significant CIP amplitudes which can dominate any such correlations. We exclude here the great earthquakes and focus the analysis on strong and major earthquakes.

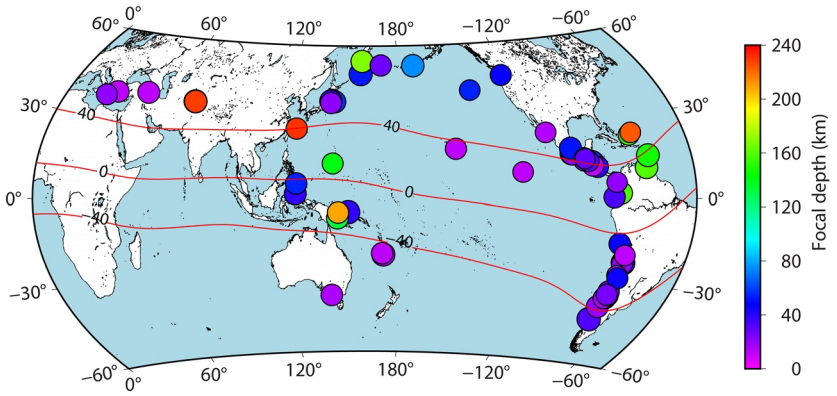

Figure 1. Epicenter locations of studied events. The color of discs represents corresponding focal depths. For more details, see Table 1 and Table S1. Red contours represent geomagnetic inclination angles −40°, 0°, and 40°.

2. Data and Methodology

The database of this study includes 59 dip-slip earthquakes that occurred during the span of last 20 years. The moment magnitude of these events ranges between 6.6 and 7.7. As aforesaid, the present study includes strong (Mw 6–Mw 6.9) to major (Mw 7–Mw 7.9) magnitude events. Figure 1 illustrates the epicentral locations of these events along with their respective focal depth. More details on the studied events such as magnitude, date, time, epicenter location, and depth are summarized in Table 1 and Table S1. The earthquake properties are obtained from Harvard CMT solutions (Dziewonski et al., 1981; Ekström et al., 2012). Table 1 lists the events during which ionospheric perturbations were detected.

Table 1
Earthquake Events With Detectable Coseismic Ionospheric Perturbation

Sr. no.	Date (dd/mm/yy)	GCMT(Mw)	Time(UTC)	GCMT Epicenter	GCMT Depth (km)	Maximum vertical displacement (cm)	Maximum CIP amplitude (TECU)
1	14/11/07	7.7	15:40:50	22.64°S, 70.62°W	37.6	235.59	0.421
2	13/01/01	7.7	17:33:32	12.97°N, 89.13°W	56	194.98	0.289
3	25/12/16	7.6	14:22:27	43.41°S, 74.43°W	32.8	180.24	0.282
4	20/03/12	7.5	18:02:47	16.60°N, 98.39°W	15.4	165.45	0.273
5	05/12/18	7.5	04:18:08	21.95°S, 169.25°E	17.8	232.17	0.492
6	05/05/15	7.5	01:44:06	5.32°S, 152.1°E	38.3	126.2	0.369
7	07/11/12	7.4	16:35:46	14.11°N, 92.43°W	21.3	129.87	0.347
8	21/08/18	7.3	21:31:47	10.76°N, 63.05°W	159.9	5.3	0.136
9	09/03/11	7.3	2:45:20	38.56°N, 142.78°E	14.1	92.44	0.350
10	07/12/12	7.2	8:18:23	38.01°N, 144.09°E	57.8	17.74	0.155
11	02/01/11	7.1	20:20:17	38.71°S, 73.84°W	19.4	39.62	0.186
12	25/03/12	7.1	22:37:06	35.31°S, 72.41°W	33.8	23.20	0.148
13	23/10/11	7.1	10:41:23	38.64°N, 43.40°E	12	67.57	0.165
14	25/09/13	7	16:42:43	16.03°S, 74.81°W	46.1	12.25	0.142
15	19/11/17	7	22:43:29	21.45°S, 168.67°E	12	52.38	0.217
16	15/11/07	6.8	15:05:58	22.98°S, 70.94°W	20.7	12.20	0.126
17	16/03/14	6.7	21:16:29	19.94°S, 70.92°W	12	14.04	0.354
18	29/09/19	6.7	15:57:53	35.56°S, 73.1°W	16.7	9.36	0.188
19	30/04/06	6.6	19:17:14	27.17°S, 71.52°W	15.4	7.05	0.132

Since the vertical surface displacement associated with strike-slip events are significantly smaller than that of dip-slip events, we do not consider strike-slip events in this study. Moreover, to keep the background ionospheric density at sufficient level, we only consider day-time events (Local time between 9 a.m. and 6 p.m.). To better resolve the dependence of CIP amplitudes on focal depth, the data set includes both shallow and intermediate depth earthquakes. Based on the depth, the earthquakes can be categorized into shallow (focal depth < 70 km), intermediate (70 km < focal depth < 300 km), and deep earthquakes (focal depth > 300 km) (Lowrie, 2007). The focal depth of the events selected in the present study varies between 12 and 230.6 km.

TEC derived from GPS data is a powerful tool to study CIP characteristics globally (e.g., Calais & Minster, 1995). Dual frequency GPS data from GPS sites located in the near field of respective earthquake epicenters (epicentral distance within ~500 km) are extracted. International GNSS Service (IGS), GPS Earth Observation NETwork (GEONET) in Japan, National Seismological Center in Chile, and Geological hazard information for New Zealand (GeoNet) construct the GPS database used in this study. Based on the obtained GPS data, TEC values are estimated using the formula

$$\mathrm{sTEC} = \frac{1}{40.3}\left(\frac{f_1^2 f_2^2}{f_1^2 - f_2^2}\right)\left(L_1\lambda_1 - L_2\lambda_2\right), \tag{1}$$

where $f_1 = 1{,}575.42$ MHz and $f_2 = 1{,}227.60$ MHz are the carrier frequencies, λ_1 and λ_2 are the corresponding wavelengths and L_1 and L_2 are the carrier phase measurements.

TEC measurements by satellites with elevation <20° are omitted. To highlight the CIP signatures, a band pass filter of 2–8 mHz is applied to sTEC and then the detrended TEC (dTEC) is converted to vertical dTEC by applying the mapping function (Mannucci et al., 1993)

$$M = \left[1 - \left(\frac{\cos(E)}{1 + h/R_E}\right)^2\right]^{1/2} \tag{2}$$

$$\text{vertical dTEC} = \text{slant dTEC} \times M \tag{3}$$

where h represents the ionospheric piercing point (IPP) height, E is the satellite elevation angle, and R_E is the Earth radius.

3. Results

The atmospheric acoustic wave perturbations due to the sudden coseismic crustal deformation generally introduce N-waves or inverted N-waves in GPS-TEC time series (Astafyeva & Heki, 2009; Astafyeva et al., 2013). Since these waves propagate with acoustic velocity in the atmosphere, they appear ~10 min after the earthquake (Bagiya et al., 2020; Heki & Ping, 2005; Rolland et al., 2011; Sunil et al., 2015; Thomas et al., 2018). In this report, TEC time series from GPS sites located in the near field of earthquake are examined for CIP signatures. The peak-to-peak amplitude of signals in vertical dTEC time series are estimated and the station-satellite pairs with maximum CIP amplitudes are identified. These observations are summarized in Table 1. As per our analysis, out of 59 earthquakes, CIP signatures are present during 19 events and absent during the remaining 40, which we caption as no-CIP events and list it in supplementary Table S1.

The moment magnitudes of no-CIP events vary between Mw 6.6 and Mw 7.5. Perevalova et al. (2014) reported the threshold magnitude of earthquakes to generate detectable signals in GPS TEC near Mw 6.5. The events they considered did not show any significant depth variations thus they could not study the effects of focal depth on CIP amplitudes. It could be noticed from Table S1 that CIP are absent for earthquakes with magnitudes in the range of 6.6–7.5.

The CIP time series during 19 events (Table 1) are illustrated in Figure 2a. Tracks of corresponding ionospheric piercing points (IPP) are shown in Figure 2b. The IPP trajectories are projected at the maximum

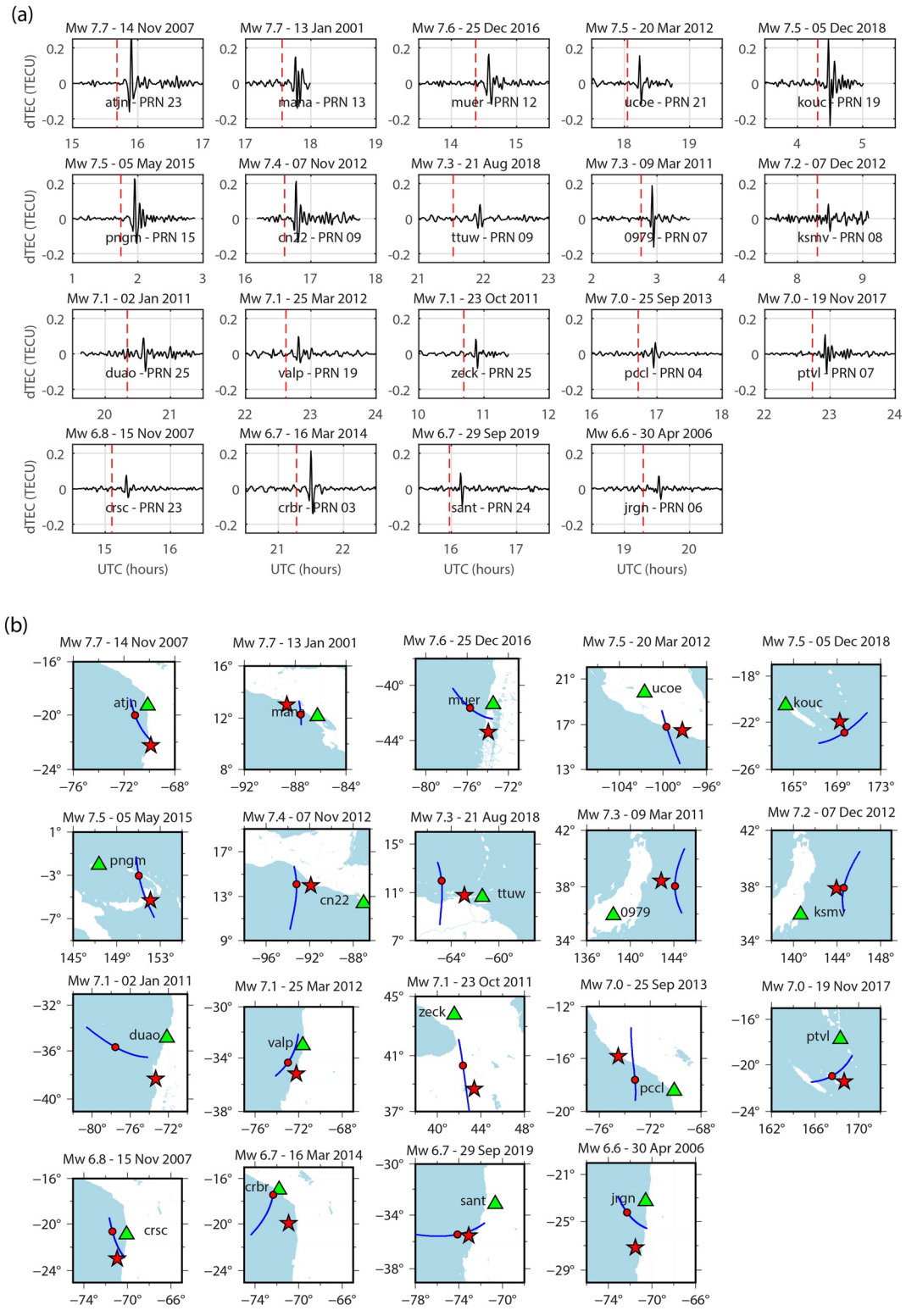

Figure 2. (a) Vertical dTEC variations. A band pass filter of 2–8 mHz is applied to slant TEC time series and then the detrended TEC values are converted to vertical dTEC. The vertical dashed lines indicate the earthquake onset. (b) Trajectories of ionospheric piercing points (IPP) in which maximum CIP amplitude is observed. Green triangle represents the location of corresponding GPS station. The red disk in each track shows the onset of CIP. Red star depicts the epicenter location. dTEC, detrended total electron content.

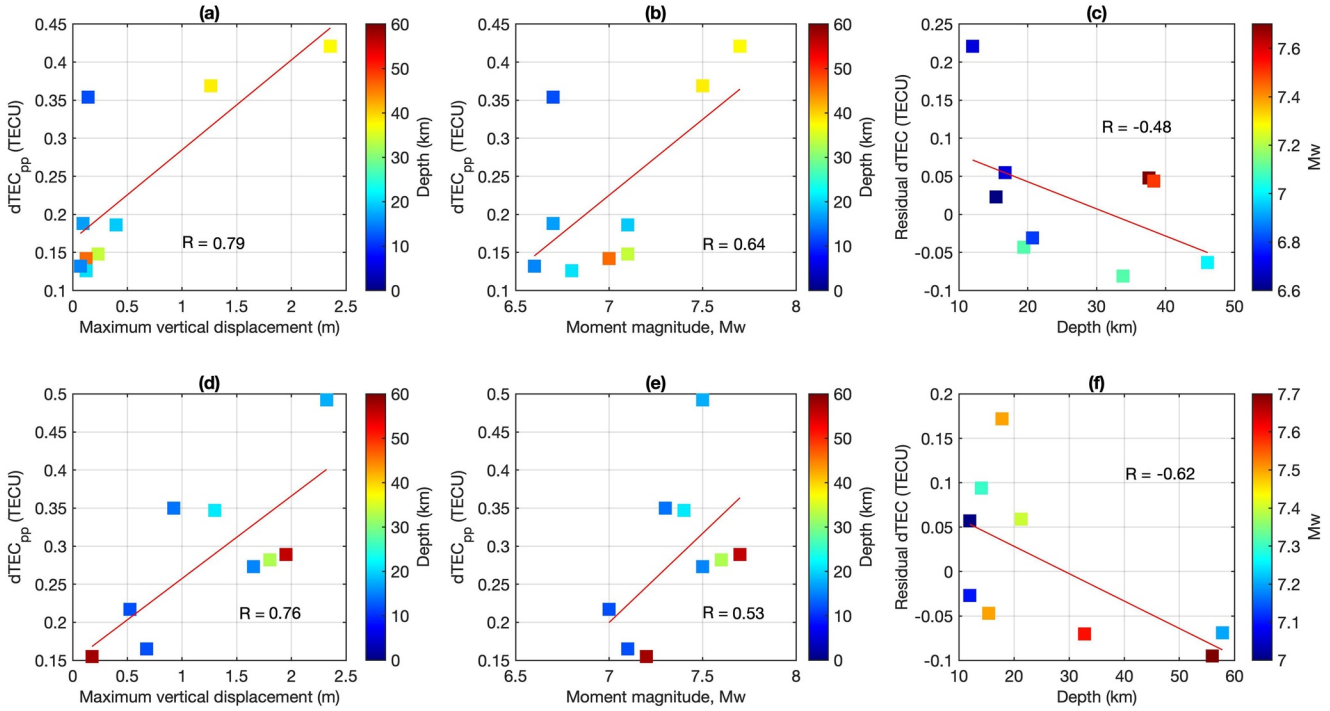

Figure 3. Correlation analysis (a) and (d) maximum vertical displacement and peak to peak dTEC amplitude (b) and (e) moment magnitude and dTEC amplitude (c) and (f) focal depth and residual vertical dTEC amplitude. In (c) and (f), the magnitude dependency in dTEC amplitudes is removed by subtracting the linear trend of (b) and (e), respectively. Corresponding correlation coefficients (R) are shown in each subfigure. Top panels include events occurred within geomagnetic inclination angle ±40° and the bottom panels consists of events occurred beyond ±40°. dTEC, detrended total electron content.

electron density altitudes at earthquake occurrence date and time obtained from the IRI model (Bilitza et al., 2017) during each event. Signals are observed for both the extreme magnitude earthquakes (Mw 7.7 and Mw 6.6) of our data set. The Mw 7.7, November 14, 2007 earthquake and Mw 7.7, January 13, 2001 earthquake are the highest magnitude events in this study. Maximum peak-to-peak CIP amplitude of ∼0.42 TECU and ∼0.29 TECU were observed from station-satellite pair atjn-PRN 23 and mana-PRN 13, respectively during these events. The focal depths of these events were 37.6 and 56 km, respectively. However, the maximum CIP amplitude in our data set is ∼0.49 TECU which was observed after the Mw 7.5, December 5, 2018 earthquake. The corresponding focal depth was 17.8 km. The lowest magnitude event with detectable CIP in this study is Mw 6.6 earthquake (focal depth 15.4 km), which occurred on April 30, 2006. Following this event, PRN 06 recorded CIP amplitude of ∼0.13 TECU from jrgn station. For these 19 events that generated detectable CIP, the focal depth varies between 12 and 159.9 km.

To investigate the possible relationship between maximum vertical displacement and dTEC amplitude, we evaluate these parameters for the events of Table 1 and demonstrate it in Figure 3. The vertical displacements are modeled using Okada's implementation (Okada, 1985) of the analytical solution of Mansinha and Smylie (1971) for a shear dislocation along an inclined fault imbedded in an elastic uniform half space. A more realistic spherical Earth model may marginally impact the displacement output. We estimate the fault length (L) and width (W) as well as the average slip (S) of each event using the empirical scaling law of Wells and Coppersmith (1994):

$$L = 10^{(Mw-4.38)/1.49}, \tag{4}$$

$$W = 10^{(Mw-4.06)/2.25}, \tag{5}$$

$$S = 10^{(Mw-6.93)/0.82}, \tag{6}$$

The estimated maximum vertical displacements are summarized in Table 1. For an estimated vertical displacement of 5.3 cm (associated with the Mw 7.3, August 21, 2018 earthquake), which is the minimum among the studied events (Table 1), CIP with amplitude of 0.136 TECU were detected. At the same time, the maximum vertical displacement of 235.59 cm generated a CIP amplitude of ∼0.42 TECU associated with the Mw 7.7, November 14, 2007 earthquake. The correlation between maximum vertical displacement and CIP amplitude is presented in Figure 3. We restrict the correlation in Figure 3 to focal depth of 60 km. There is only one event that occurred at focal depths beyond 60 km which could generate detectable CIP. To account for the possible effect of ambient ionospheric electron density variations on CIP amplitudes, we have categorized the data set based on the geomagnetic inclination angle at epicenters into (a) events occurred within ±40° (low latitude events) and (b) events occurred beyond ±40°. From Figures 3a and 3d, the anticipated positive correlation can be clearly observed. The estimated correlation coefficients are $R = 0.79$ and $R = 0.76$, respectively.

However, as mentioned, coseismic surface displacement is controlled by various seismic parameters of moment magnitude, focal mechanism, depth etc (Bonilla, 1988; Wells & Coppersmith, 1994). We explore the dependence of the observed CIP amplitudes on other seismic source parameters. The significant positive correlation ($R = 0.64$ and $R = 0.53$) between CIP amplitudes and earthquake magnitude (Figures 3b and 3e) corroborates well with the earlier studies by Astafyeva et al. (2013) and Cahyadi and Heki (2015). It can be noticed that the correlation of CIP amplitudes with maximum vertical displacement is stronger than that with moment magnitude. In other words, CIP amplitudes are sensitive to the wavelength of surface deformation. Uplift concentrated in a small region appears more efficient at producing CIP than distributed uplift. Since the surface deformation is a function of focal depth, this observation opens the discussion about the role of focal depth on CIP amplitudes.

We now explore the response of CIP amplitudes to focal depth. To do this, we first removed the magnitude dependency in CIP amplitudes. The simple model which can define the relation between moment magnitude and CIP amplitude is a linear model deduced by linear regression. To eliminate the magnitude dependency, this linear trend is removed from the vertical dTEC. The resultant residual dTEC along with the focal depth are shown in Figures 3c and 3f. A significant negative correlation ($R = -0.48$ and $R = -0.62$) conveys that deeper earthquakes are less efficient at producing ionospheric perturbations.

4. Discussion

The coseismic vertical displacement at the Earth surface, which is considered as the main source of CIP, depends on various earthquake source parameters. The earthquake size and focal depth largely influence the coseismic surface deformation (Bonilla, 1988). The earthquake size in terms of moment magnitude is defined by the fault area, average fault displacement, and shear modulus (Fowler, 2005; Hanks & Kanamori, 1979). According to Wells and Coppersmith (1994), size and focal depth of earthquakes together with the properties of near-surface materials considerably affect the surface faulting. By studying 31 shallow earthquakes, Bonilla (1988) reported the minimum magnitude of ∼M 5 to generate surface faulting. Wells and Coppersmith (1994) showed that the moment magnitude and maximum displacement are linked by an empirical relation $\log(MD) = -5.46 + 0.82 \times \mathrm{M}$, where M is the the moment magnitude and MD is the maximum displacement in meter.

Apart from magnitude, the depth of rupture surface is an important factor affecting the surface faulting (Bonilla, 1988). Larger focal depths reduce the possibility of appearance of subsurface displacements at the surface. Gutenberg (1956) formulated the seismic energy released during earthquakes based on their magnitudes that is, $\log E = 5.8 + 2.4M$, where E is the energy and M is the unified magnitude. They also showed that the energy released decreases nearly exponentially with increasing focal depth. However, during shallow and intermediate earthquakes, the energy reduced very gradually. Considering the variations in moment magnitude and focal depth, large magnitude and shallow earthquakes are more probable to introduce significant ground motion than that of small magnitude and deep earthquakes (Otsuka, 1964).

In this study, we examine the distinct effects of (1) maximum vertical ground displacement, (2) moment magnitude, and (3) focal depth on CIP amplitudes. Accordingly, we first estimated the relation between the maximum vertical displacement and CIP amplitude. The strong correlation, $R = 0.79$ and $R = 0.76$,

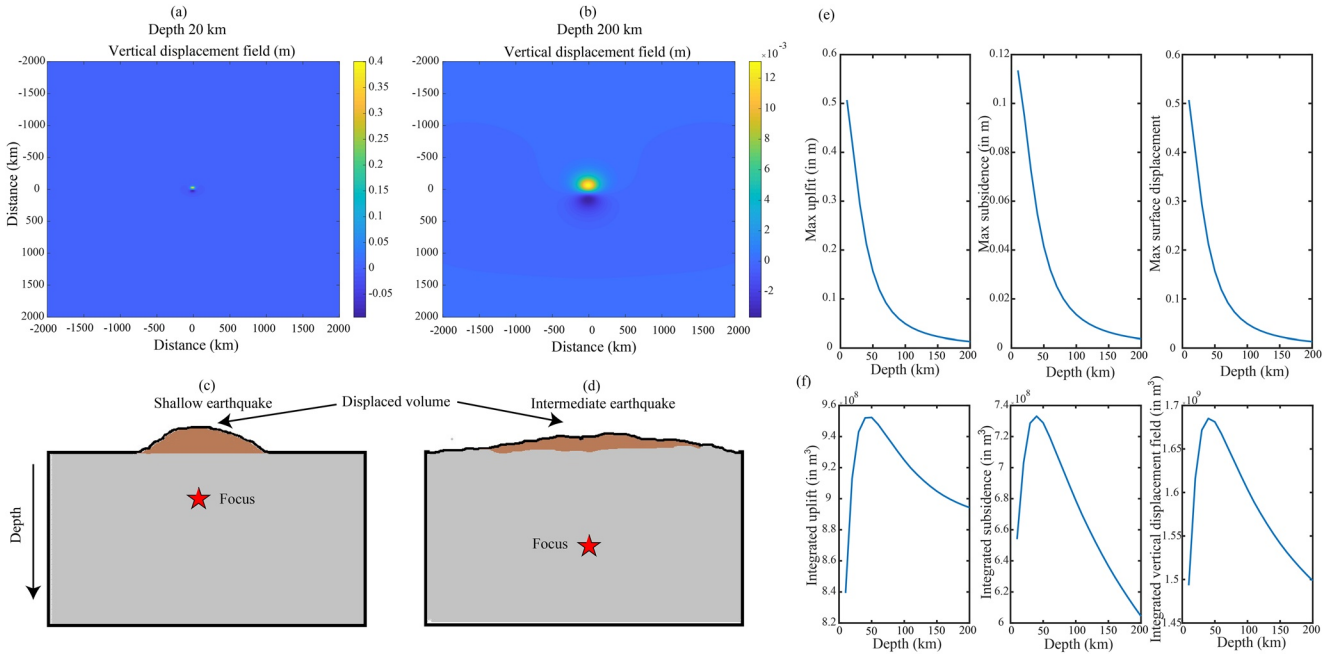

Figure 4. Synthetic test illustrating the variation of coseismic ground deformations with focal depth. Pure dip-slip earthquakes are considered with magnitude of Mw 7.2 and dip angle 20°. (a) Vertical ground displacement when the focal depth is 20 km. Maximum vertical displacement estimated is ~0.4 m. (b) When the focus is shifted to 200 km depth. Maximum uplift is reduced to ~0.013 m in this case. (c) and (d) represent the displacement fields for different focal depths; (e) and (f) show the synthetic test results for a depth range of 10–200 km; (e) shows the maximum uplift, subsidence and vertical surface displacements. The maximum displacement fields decrease logarithmically with increasing focal depth; and (f) shows the integrated displacement fields (volumes of the uplifted/subsided material) which do not change significantly with depth.

indicates that CIP amplitudes are indeed linked to the vertical ground displacement. As discussed, the ground displacement is a function of magnitude, focal depth and focal mechanism. Our analysis further suggests that the CIP amplitude increases with moment magnitude. In our data set, these two parameters correlate similarly ($R = 0.64$ and $R = 0.53$).

We investigate the effect of focal depth on CIP amplitudes by considering 18 events (focal depth within 60 km) (Table 1). We have considered only daytime and dip-slip events occurred during the past 20 years. These restrictions limit the focal depth of studied events between 12 and 57.8 km. Thus, the studied events fall in the categories of shallow depth earthquakes. The ionospheric response to earthquakes with focal depths > 60 km could not be analyzed in this study. The focal depths and residual dTEC (CIP amplitudes corrected for earthquake magnitude dependency) exhibits negative correlations with $R = -0.48$ and $R = -0.62$, meaning that deep earthquakes are less efficient at generating CIP.

We have performed a synthetic test to understand how the focal depth affects the deformations at the surface and thus the CIP amplitudes. We considered two pure dip-slip earthquakes, one at 20 km depth, the other at 200 km. The event moment magnitude is considered as 7.2 and a dip angle of 20°. The maximum vertical ground displacement and total volume of the uplifted/subsided region are estimated using Okada's analytical solution for a shear dislocation imbedded in an elastic uniform half space (Okada, 1985). Panels (a) and (b) in Figure 4 show the results of this synthetic test. When the event depth is 20 km, a small area above the hypocenter is deformed with large values of vertical displacement. In this case, the maximum vertical displacement estimated is ~0.4 m. When the depth is shifted to 200 km, the extent of the deformed area increases and the maximum value of vertical displacement reduces. The maximum uplift is reduced to ~0.013 m in this case. Figures 4c and 4d schematically depict the displacement fields for different focal depths. The displaced volume (brown shaded region) remains nearly the same. What changes is the repartition, concentrated in a narrow area for shallow earthquakes, spread over very wide areas for deep ones. A more realistic spherical Earth model in place of Okada (1985) may marginally impact the derived vertical displacement but would not change the conclusion of the synthetic test.

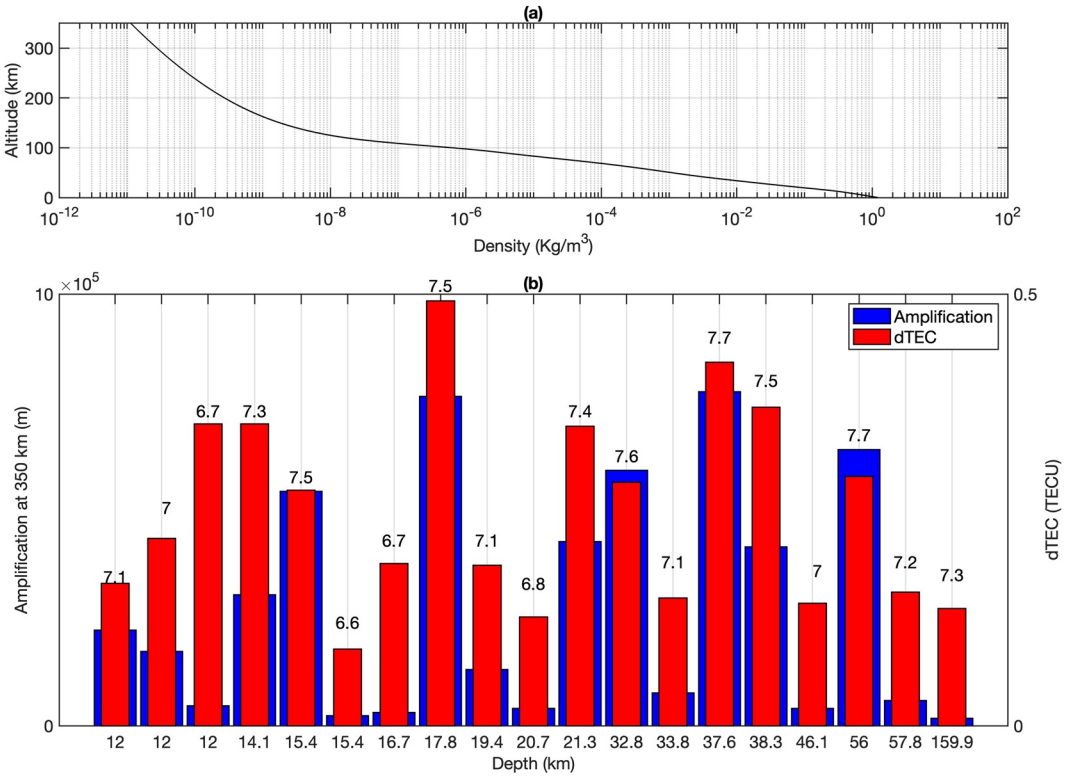

Figure 5. (a) Altitudinal variation of atmospheric neutral density derived from NRLMSISE-00 model. (b) Amplification of seismic energy transferred into the atmosphere by maximum ground displacement at an altitude of 350 km. The blue bars show the amplification at this height and the red bars show the corresponding vertical dTEC amplitude. dTEC, detrended total electron content.

The result of a synthetic test for a depth range of 10–200 km is shown in the right panels in Figure 4. The top panel (e) shows the maximum uplift, subsidence and surface displacement. The estimated maximum displacement fields decrease logarithmically with increasing focal depth. On the contrary, the integrated volume of the uplifted/subsided material does not change significantly with depth (Figure 4f). In short, shallow earthquakes generate significant surface displacements concentrated in a smaller region and deep earthquakes generate comparatively smaller surface displacements distributed over a wide region. The small-scale ground deformations during deep earthquakes may not transfer sufficient seismic energy into the overlying atmosphere to generate detectable ionospheric electron density perturbations.

The observed CIP sensitivity on the wavelength of the displacement field might bring constraints on the physics of the phenomenon that would be worth investigating in future work. The Next Generation Gravity Mission (NGGM) to be launched by the European Space Agency (Cambiotti et al., 2020) might allow comparison with earthquake-induced gravity signals on a comparable set of earthquakes.

The acoustic waves triggered by an earthquake when propagate to atmospheric altitudes, they amplify exponentially (Lognonné et al., 1998). The amplification is due to the combined effect of (1) the conservation of energy, ρv^2 that transferred to the atmosphere during seismic events and (2) the exponential decrease in atmospheric density, ρ with altitude (Artru et al., 2004; Occhipinti, 2015). The altitudinal variation of atmospheric neutral density derived from NRLMSISE-00 model (Picone et al., 2002) is shown in Figure 5a. At atmospheric height of 350 km, the density changes by 10 orders as seen from the figure, this can produce amplification up to five orders. However, dissipative effects due to viscous damping become significant above 100 km altitude (Artru et al., 2001; Pitteway & Hines, 1963).

We have computed the atmospheric amplification of seismic energy in terms of maximum vertical ground displacement and listed in Table 1. Chum et al. (2012) presented a comprehensive study of infrasound amplification in the atmosphere. However, here we follow a simple calculation to find the unattenuated

amplification of seismic energy transferred into the atmosphere by co-seismic ground displacements. The amplification factor at a given altitude is estimated using the formula, $\text{Amplification factor} = \sqrt{\frac{\rho_0}{\rho_z}}$, where ρ_0 is the atmospheric density at ground level and ρ_z is the density at the respective altitude (Garcia et al., 2005). The effects of viscosity are not considered in this calculation. The blue bars in Figure 5b represent the amplification at 350 km of atmospheric altitude and the red bars show the corresponding vertical dTEC amplitude. The lowest value which generated detectable CIP is 1.74×10^4 m, corresponding to the Mw 7.3, August 21, 2018 earthquake. The focal depth associated with this event is 159.9 km. A precise cut off which can generate detectable CIP is not clear from the current data set. Inclusion of more events by relaxing the constraints of focal mechanisms and time of occurrence may improve the results.

5. Conclusion

The distinct effects of seismic source parameters such as vertical ground displacement, moment magnitude and focal depth on CIP amplitudes are investigated. We have analyzed the ionospheric response to 59 dip-slip earthquakes that occurred in the past 20 years. Based on this, the maximum vertical ground displacement and moment magnitude correlates well with the CIP amplitudes. One of the major finding in this study is the dependence of CIP amplitude on focal depth. By analyzing earthquakes with varying depths, we found that deep earthquakes manifest with smaller CIP. The reason for this negative dependence is attributed to the corresponding maximum vertical displacement. Synthetic tests highlight that when the focal depth increases, the associated maximum vertical displacement decreases, which in turn reduces the CIP amplitudes.

Data Availability Statement

Data sets for this research are available from UNAVCO (https://www.unavco.org/data/gps-gnss/gps-gnss.html), Geospatial Information Authority of Japan (https://terras.gsi.go.jp), National Seismological Center in Chile (http://gps.csn.uchile.cl/data/) and Geological hazard information for New Zealand (https://www.geonet.org.nz/data/types/geodetic).

Acknowledgments
A. S. Sunil sincerely thank the Department of Science and Technology (DST), Govt. of India for the research associate fellowship. This work is part of the interdisciplinary program "Coupled Lithosphere-Atmosphere-Ionosphere-Magnetosphere System (CLAIMs)" of Indian Institute of Geomagnetism and supported by DST, India. This work has been supported by the French government, through the UCA JJEDI Investments in the Future project managed by the National Research Agency (ANR) ANR-15-IDEX-01 and by the ANR research grants ITEC (ANR-19-CE04-003).

References

Artru, J., Farges, T., & Lognonné, P. (2004). Acoustic waves generated from seismic surface waves: Propagation properties determined from Doppler sounding observations and normal-mode modeling. *Geophysical Journal International*, *158*, 1067–1077. https://doi.org/10.1111/j.1365-246X.2004.02377.x

Artru, J., Lognonné, P., & Blanc, E. (2001). Normal modes modeling of post-seismic ionospheric oscillations. *Geophysical Research Letters*, *28*, 697–700. https://doi.org/10.1029/2000GL000085

Astafyeva, E. I., & Heki, K. (2009). Dependence of wave form of near-field coseismic ionospheric disturbances on focal mechanisms. *Earth Planets and Space*, *61*, 939–943. https://doi.org/10.1186/BF03353206

Astafyeva, E. I., Rolland, L. M., & Sladen, A. (2014). Strike-slip earthquakes can also be detected in the ionosphere. *Earth and Planetary Science Letters*, *405*, 180–193. https://doi.org/10.1016/j.epsl.2014.08.024

Astafyeva, E. I., Shalimov, S., Olshanskaya, E., & Lognonné, P. (2013). Ionospheric response to earthquakes of different magnitudes: Larger quakes perturb the ionosphere stronger and longer. *Geophysical Research Letters*, *40*, 1675–1681. https://doi.org/10.1002/grl.50398

Bagiya, M. S., Sunil, A. S., Rolland, L., Nayak, S., Ponraj, M., Thomas, D., & Ramesh, D. S. (2019). Mapping the impact of non-tectonic forcing mechanisms on GNSS measured coseismic ionospheric perturbations. *Scientific Reports*, *9*, 1–15. https://doi.org/10.1038/s41598-019-54354-0

Bagiya, M. S., Sunil, A. S., Sunil, P. S., Sreejith, K. M., Rolland, L. M., & Ramesh, D. S. (2017). Efficiency of coseismic ionospheric perturbations in identifying crustal deformation pattern: Case study based on Mw 7.3 May Nepal 2015 earthquake. *Journal of Geophysical Research: Space Physics*, *122*, 6849–6857. https://doi.org/10.1002/2017JA024050

Bagiya, M. S., Sunil, P. S., Sunil, A. S., & Ramesh, D. S. (2018). Co-seismic contortion and coupled nocturnal ionospheric perturbations during 2016 Kaikoura, Mw 7.8 New Zealand earthquake. *Journal of Geophysical Research: Space Physics*, *123*, 1–11. https://doi.org/10.1002/2017JA024584

Bagiya, M. S., Thomas, D., Astafyeva, E., Bletery, Q., Lognonné, P., & Ramesh, D. S. (2020). The ionospheric view of the 2011 Tohoku-Oki earthquake seismic source: The first 60 seconds of the rupture. *Scientific Reports*, *10*, 1–15. https://doi.org/10.1038/s41598-020-61749-x

Bilitza, D., Altadill, D., Truhlik, V., Shubin, V., Galkin, I., Reinisch, B., & Huang, X. (2017). International Reference Ionosphere 2016: From ionospheric climate to real-time weather predictions. *Space Weather*, *15*, 418–429. https://doi.org/10.1002/2016SW001593

Bonilla, M. G. (1988). Minimum earthquake magnitude associated with coseismic surface faulting. *Bulletin of the Association of Engineering Geologists*, *25*, 17–29. https://doi.org/10.2113/gseegeosci.xxv.1.17

Cahyadi, M. N., & Heki, K. (2015). Coseismic ionospheric disturbance of the large strike-slip earthquakes in North Sumatra in 2012: Mw dependence of the disturbance amplitudes. *Geophysical Journal International*, *200*, 116–129. https://doi.org/10.1093/gji/ggu343

Calais, E., & Minster, J. B. (1995). GPS detection of ionospheric perturbations following the January 17, 1994, northridge earthquake. *Geophysical Research Letters*, *22*, 1045–1048. https://doi.org/10.1029/96GL01256

Cambiotti, G., Douch, K., Cesare, S., Haagmans, R., Sneeuw, N., Anselmi, A., et al. (2020). On Earthquake Detectability by the Next-Generation Gravity Mission. *Surveys in Geophysics*, *41*, 1049–1074. https://doi.org/10.1007/s10712-020-09603-7

Chum, J., Hruska, F., Zednik, J., & Lastovicka, J. (2012). Ionospheric disturbances (infrasound waves) over the Czech Republic excited by the 2011 Tohoku earthquake. *Journal of Geophysical Research*, *117*, 1–13. https://doi.org/10.1029/2012JA017767

Davies, K., & Baker, D. M. (1965). Ionospheric effects observed around the time of the Alaskan earthquake of March 28, 1964. *Journal of Geophysical Research*, *70*, 2251. https://doi.org/10.1029/JZ070i009p02251

Dziewonski, A. M., Chou, T. A., & Woodhouse, J. H. (1981). Determination of earthquake source parameters from waveform data for studies of global and regional seismicity. *Journal of Geophysical Research*, *86*, 2825–2852. https://doi.org/10.1029/JB086iB04p02825

Ekström, G., Nettles, M., & Dziewoński, A. M. (2012). The global CMT project 2004-2010: Centroid-moment tensors for 13,017 earthquakes. *Physics of the Earth and Planetary Interiors*, *200–201*, 1–9. https://doi.org/10.1016/j.pepi.2012.04.002

Fowler, C. M. R. (2005). *The solid earth: An introduction to global geophysics*. Cambridge University Press. https://doi.org/10.1017/CBO9780511819643

Garcia, R., Lognonné, P., & Bonnin, X. (2005). Detecting atmospheric perturbations produced by Venus quakes. *Geophysical Research Letters*, *32*, 1–4. https://doi.org/10.1029/2005GL023558

Georges, T. M., & Hooke, W. H. (1970). Wave-induced fluctuations in ionospheric electron content - A model indicating some observational biases. *Journal of Geophysical Research*, *75*, 6295–6308. https://doi.org/10.1029/JA075i031p06295

Gutenberg, B. (1956). The energy of earthquakes. *Quarterly Journal of the Geological Society*, *112*(1-4), 1–14. https://doi.org/10.1144/gsl.jgs.1956.112.01-04.02

Hanks, T. C., & Kanamori, H. (1979). A moment magnitude scale. *Journal of Geophysical Research*, *84*, 2348–2350.

Heki, K., Otsuka, Y., Choosakul, N., Hemmakorn, N., Komolmis, T., & Maruyama, T. (2006). Detection of ruptures of Andaman fault segments in the 2004 great Sumatra earthquake with coseismic ionospheric disturbances. *Journal of Geophysical Research*, *111*, 1–11. https://doi.org/10.1029/2005JB004202

Heki, K., & Ping, J. (2005). Directivity and apparent velocity of the coseismic ionospheric disturbances observed with a dense GPS array. *Earth and Planetary Science Letters*, *236*, 845–855. https://doi.org/10.1016/j.epsl.2005.06.010

Lognonné, P., Clevede, E., & Kanamori, H. (1998). Computation of seismograms and atmospheric oscillations by normal-mode summation for a spherical earth model with realistic atmosphere. *Geophysical Journal International*, *135*, 388–406. https://doi.org/10.1046/j.1365-246X.1998.00665.x

Lognonné, P., & Garcia, R. (2006). Seismic waves in the ionosphere. *Europhysics News*, *37*, 11–14. https://doi.org/10.1051/epn:2006401

Lowrie, W. (2007). *Fundamentals of geophysics* (2nd ed.). Cambridge University Press. https://doi.org/10.1017/CBO9780511807107

Mannucci, A. J., Wison, B. D., & Edwards, C. D. (1993). A new method for onitoring the Earth's ionospheric total electron content using GPS global networks. *Proceedings of ION GPS-93*, *93*, 1323–1332.

Mansinha, L., & Smylie, D. E. (1971). The displacement fields on inclined faults. *Bulletin of the Seismological Society of America*, *61*, 1433–1440.

Occhipinti, G. (2015). The seismology of the Planet Mongo: The 2015 ionospheric seismology review. *Subduction dynamics: From mantle flow to mega disasters* (pp. 169–182). https://doi.org/10.1002/9781118888865.ch9

Okada, Y. (1985). Surface deformation due to shear and tensile faults in a half-space. *Bulletin of the Seismological Society of America*, *75*, 1135–1154. https://doi.org/10.1016/0148-9062(86)90674-1

Otsuka, M. (1964). Earthquake magnitude and surface fault formation. *Journal of Physics of the Earth*, *12*. https://doi.org/10.4294/zisin1948.18.1_1

Perevalova, N. P., Sankov, V. A., Astafyeva, E. I., & Zhupityaeva, a. S. (2014). Threshold magnitude for ionospheric response ionospheric TEC response to earthquakes. *Journal of Atmospheric and Solar-Terrestrial Physics*, *108*, 77–90. https://doi.org/10.1016/j.jastp.2013.12.014

Picone, J. M., Hedin, A. E., Drob, D. P., & Aikin, A. C. (2002). NRLMSISE-00 empirical model of the atmosphere: Statistical comparisons and scientific issues. *Journal of Geophysical Research*, *107*(A12), 1–16. https://doi.org/10.1029/2002JA009430

Pitteway, M. L. V., & Hines, C. O. (1963). The viscous damping of atmospheric gravity waves. *Canadian Journal of Physics*, *41*(1903). https://doi.org/10.1139/p63-194

Rolland, L. M., Lognonné, P., Astafyeva, E. I., Kherani, E. A., Kobayashi, N., Mann, M., & Munekane, H. (2011). The resonant response of the ionosphere imaged after the 2011 off the Pacific coast of Tohoku Earthquake. *Earth Planets and Space*, *63*, 853–857. https://doi.org/10.5047/eps.2011.06.020

Rolland, L. M., Vergnolle, M., Nocquet, J. M., Sladen, A., Dessa, J. X., Tavakoli, F., et al. (2013). Discriminating the tectonic and non-tectonic contributions in the ionospheric signature of the 2011, Mw7.1, dip-slip Van earthquake, Eastern Turkey. *Geophysical Research Letters*, *40*, 2518–2522. https://doi.org/10.1002/grl.50544

Sunil, A. S., Bagiya, M. S., Catherine, J., Rolland, L. M., Sharma, N., Sunil, P. S., & Ramesh, D. S. (2017). Dependence of near field co-seismic ionospheric perturbations on surface deformations: A case study based on the April, 25 2015 Gorkha Nepal earthquake. *Advances in Space Research*, *59*, 1200–1208. https://doi.org/10.1016/j.asr.2016.11.041

Sunil, A. S., Bagiya, M. S., Reddy, C. D., Kumar, M., & Ramesh, D. S. (2015). Post-seismic ionospheric response to the 11 April 2012 East Indian Ocean doublet earthquake. *Earth Planets and Space*, *67*, 37. https://doi.org/10.1186/s40623-015-0200-8

Thomas, D., Bagiya, M. S., Sunil, P. S., Rolland, L., Sunil, A. S., Mikesell, T. D., et al. (2018). Revelation of early detection of co-seismic ionospheric perturbations in GPS-TEC from realistic modeling approach: Case study. *Scientific Reports*, *8*, 1–10. https://doi.org/10.1038/s41598-018-30476-9

Watada, S., & Kanamori, H. (2010). Acoustic resonant oscillations between the atmosphere and the solid earth during the 1991 Mt. Pinatubo eruption. *Journal of Geophysical Research*, *115*, 1–20. https://doi.org/10.1029/2010JB007747

Wells, D. L., & Coppersmith, K. J. (1994). New empirical relationships among magnitude, rupture length, rupture width, rupture area, and surface displacement. *Bulletin of the Seismological Society of America*, *84*, 974–1002.